# Precise energy determination of Ni $K\alpha$ and Fe $K\beta$ in high ionization states using a microcalorimeter

Marc Botz [1,2] Luciano Gottardi [3] Martin de Wit [3] Chintan Shah [4,1,5] Liyi Gu [3,6] François Pajot [7] Thomas Pfeifer [1] and José R. Crespo López-Urrutia [1]

[1] *Max-Planck-Institut für Kernphysik, Saupfercheckweg 1, 69117 Heidelberg, Germany*

[2] *Heidelberg Graduate School for Physics, Ruprecht-Karls-Universität Heidelberg, Im Neuenheimer Feld 226, 69120 Heidelberg, Germany*

[3] *SRON, Space Research Organisation Netherlands, Niels Bohrweg 4, 2333 CA Leiden, The Netherlands*

[4] *NASA/Goddard Space Flight Center, 8800 Greenbelt Road, Greenbelt, Maryland 20771, USA*

[5] *Department of Physics and Astronomy, Johns Hopkins University, Baltimore, Maryland 21218, USA*

[6] *Leiden Observatory, Leiden University, P.O. Box 9513, 2300 RA Leiden, The Netherlands*

[7] *IRAP, Université de Toulouse, CNRS, 9 Av. du Colonel Roche, 31400 Toulouse, France*

(Received 19 June 2026; accepted 21 October 2026; published 9 November 2026)

Accurate laboratory transition energies for the Ni $K_\alpha$−Fe $K_\beta$ blend are urgently needed both for atomic-structure benchmarking and interpretation of astrophysical x-ray spectra observed with space telescopes. Crucially, inferred abundances of these elements, which are essential for the diagnostics of hot plasmas, depend on the treatment of those overlapping transitions. By combining a transition-edge-sensor x-ray microcalorimeter array and a superconducting electron beam ion trap, we distinguish with line widths between 3.5 eV and 5.5 eV the key transitions from Ni XX to Ni XXVII, including previously unmeasured ones, from the $K_\beta$ lines of Fe XX to Fe XXV. Collisional-radiative calculations using the Flexible Atomic Code agree well with our results. By calibrating all sensors individually and correcting for their temporal drifts we achieve an average uncertainty below 20 km/$s$ for their transition energies, easing the interpretation of astrophysical spectra. Furthermore, our charge-state-resolved results benchmark theory for complex open-shell ions in the intermediate coupling regime, for which we compare the results from pure configuration interaction and calculations including many-body perturbation theory (MBPT) and find a significant improvement when including MBPT.

DOI: 10.1103/ynpq-nhq6

## I. INTRODUCTION

Iron and nickel are synthesized in stars at different stages of their life. Their x-ray emissions are essential for the diagnostics of hot astrophysical plasmas, including also those seen around active galactic nuclei, binary systems, and galaxy clusters. Unfortunately, the characteristic Ni $K_\alpha$ emissions are very close to the Fe XXV $K_\beta$ region, with the strongest line of Ni XXVII just 70 eV below the main lines of the Fe XXV $K_\beta$ multiplet. For lower Fe charge states, particularly Fe XXIV and Fe XXIII, multiplets of Fe $K_\beta$ and Ni $K_\alpha$ overlap and cannot be well resolved in typical observations. Only by being equipped with an accurate knowledge of the spectra of all those ions can we quantitatively separate the contributions of Ni and Fe, of which the latter is the most prominent element in x-ray astronomy. The former, nickel, is observed with space telescopes as well, e.g., with the microcalorimeter-equipped X-Ray Imaging and Spectroscopy Mission (XRISM), in many sources such as in the supernova remnant (SNR) Cassiopeia A [1], the binary star system GT Muscae [2], and the galactic neutron star binary GX13 + 1 [3], where it serves as a probe of conditions in core-collapse supernovas [4].

Despite these and many other astrophysical observations, there is a lack of high-precision laboratory data on x-ray emissions of nickel, with emissions mainly being observed following dielectronic capture. Previous measurements of dielectronic satellites of nickel in an electron beam ion trap (EBIT) lacked a high-resolution x-ray detector [5]. Dielectronic satellites were also investigated in several tokamak measurements, as in [6–9], the latter of which achieved an absolute accuracy of approximately 5 eV. In astrophysical observations, the lines are blended due to plasma conditions and finite detector resolution. Likewise, the available theoretical calculations are mostly limited to Ni XXVII [10,11] and Ni XXVI [12]. Transition energy calculations for lower charge states were performed in [13] using the Hartree-Fock with relativistic corrections method of Cowan [14]. From an atomic physics perspective, this task is demanding because open-shell highly charged ions produce dense $K$-shell multiplets, which are difficult to calculate. Charge-state-resolved, accurately calibrated laboratory measurements with an explicit treatment of uncertainties are therefore needed to benchmark such calculations.

Until now, the Fe $K_\beta$ lines blended with Ni $K_\alpha$ have not been studied in detail for charge states below Fe XXIV as well. Works on various iron charge states done at synchrotrons [15,16] and with crystal spectrometers [17] provided precise transition energies mostly for the $K_\alpha$ region. $K_\beta$ emissions from highly charged iron were studied at the synchrotron down to Fe XXIV [18] and at the tokamak down to Fe XXIII [8], whereas the $K_\beta$ emissions of lower charge states remain unexplored.

*Published by the American Physical Society under the terms of the Creative Commons Attribution 4.0 International license. Further distribution of this work must maintain attribution to the author(s) and the published article's title, journal citation, and DOI. Open access publication funded by Max Planck Society.*

This data scarcity hinders the interpretation of astrophysical observations. In the analysis of very recent XRISM data, different astrophysical codes, such as SPEX [19] and ATOMDB [20], yielded different nickel abundances due to the Ni $K_\alpha$-Fe $K_\beta$ blend [1]. Including transitions of additional charge states of both nickel and iron in those models should enable more precise abundance determinations and reduce their model dependence.

This lack of reference spectroscopy data will furthermore reduce the scientific harvest of upcoming missions, like NewAthena [21], which promises an even higher resolution than XRISM thanks to its high-resolution x-ray spectrometer X-IFU [22–24]. At lower photon energies in the soft x-ray regime, which should be accessible to NewAthena, an increasing number of outer-shell transitions additionally complicate the spectra, making laboratory data even more necessary.

Here we present high-resolution spectra of Ni $K_\alpha$ transitions from Ni XXVII to Ni XX and Fe $K_\beta$- and $K_\gamma$ transitions from Fe XXV to Fe XX excited by electron impact. The ions were produced and trapped with an electron beam ion trap, FLASH-EBIT [25,26] at the Max Planck Institut für Kernphysik (MPIK), and the spectra recorded with a high-resolution transition-edge-sensor (TES) microcalorimeter array developed at the Dutch space-science institute SRON that covers a bandwidth from 300 to 12 000 eV in the present configuration.

## II. EXPERIMENTAL SETUP

To prepare the highly charged iron and nickel ions in the desired charge states between hydrogen-like and fluorine-like, an intense electron beam is used. The 6 T superconducting Helmholtz coils surrounding the central trap chamber of the EBIT compress an electron beam with a current of 200 mA to a high density at kinetic energies set to 11 keV for the nickel and 9.5 keV for the iron measurements. Precursor iron and nickel atoms were dissociated by the electron beam from volatile compounds injected as tenuous molecular beams. At the trap center, those atoms are then ionized and subsequently trapped radially in the negative space-charge potential well generated by the dense electron beam. The required axial trapping potential is generated by cylindrical electrodes, so-called drift tubes, surrounding the trap center, by making those adjacent to the center drift tube slightly more positive than the center one.

For nickel, we inject a beam of bis(cyclopentadienyl)-nickel(II). Its vapor pressure at a temperature of 100° C provides the necessary flux through the differentially pumped injection system. For iron, we use iron pentacarbonyl [$Fe(CO)_5$] at room temperature. To observe several charge states of Fe in a single measurement, we switch off the electron beam for one second every five seconds, effectively restarting the ionization process. This lets intermediate charge states dominate at the start of each cycle, and higher ones up to Fe XXV at its end. This gives us the desired charge-state distribution in spite of the high electron beam energies needed to excite the inner-shell emissions, which otherwise would be dominated by He-like Fe. For the iron measurement we need this method since the collisional excitation cross sections for their $K_\beta$ transitions are lower than those of the Ni $K_\alpha$ transitions. For our nickel measurement it was sufficient to set the electron beam to a continuous current of 200 mA, with the trap being emptied only about once per minute to dump contaminant ions.

X rays are recorded with the SRON transition-edge-sensor-based microcalorimeter spectrometer [27], as in a recent closely related study [28]. Its principle of operation uses a superconducting element held at its critical temperature, which sees a sudden increase of resistance due to the partial transition from superconducting to normal conducting state upon absorption of an x-ray photon. This increase is proportional to the deposited energy and the concomitant, minute change of temperature. During the present experiment, each of its 34 single pixels showed a resolution of around 3 eV at 7 keV and covered the range between 300 eV and 12 000 eV with low background. For photon-energy calibration we used Fe XXVI and Fe XXV, for which transition energies are well known and close to the Ni transitions of interest. In the Ni measurement we included the w line of Ni XXVII, which is also well known and sufficiently separated from the other Ni transitions. By conducting our measurements on Ni immediately after injecting $Fe(CO)_5$, slowly out-gassing residual $Fe(CO)_5$ frozen on the cryogenic surfaces of the EBIT yielded also small but measurable Fe transitions. This allows us to calibrate also with them and follow time drifts of the detector response without interfering with the Ni lines.

## III. DATA ANALYSIS AND RESULTS

### A. Calibration and time drift correction

Overall three measurements on Ni HCI were conducted. Measurement I lasted one day and showed a strong Fe contamination that was used for calibration. The spectrum is dominated by Ni XXVII and Fe XXV. Measurement II had a moderate Fe contamination and lasted another day. Measurement III lasted five days with little Fe contamination and a broader charge-state distribution for Ni due to a higher injection pressure. The Fe campaign consisted of two measurements. First, we recorded calibration lines of Fe XXV for three days under conditions dominated by Fe XXV and Fe XXIV. About five weeks later we took data for the lower charge states by switching the electron beam off every five seconds for one second for two weeks. Charge exchange during the beam-off phase lowered the peak of the charge-state distribution.

As the microcalorimeter behaved very stably during the measurements on Fe, the pixel-averaged drift of the energy scale between the two measurements was only around 1 eV at 7 keV. During the Ni campaign however, the cryogenic system of the microcalorimeter showed instabilities caused by a pollution of the helium circuit of the dilution refrigerator cooling the detector. This led to jumps of the detector response between and drifts during individual measurements. Some pixels showed changes in the energy scale of around 10 eV for the Ni w line over two weeks, mostly consisting of jumps between measurements. We carefully monitored and corrected for this drift to maintain the calibration and high resolution over the whole measurement.

Calibrations in both campaigns were therefore carried out in several steps to account for the unique gain curve of the

TABLE I. Literature values of the calibration lines with residuals to the fitted experimental values with their statistical uncertainties and combined systematic uncertainties (individual pixel calibration, summed spectrum calibration, and time drift) of the summed spectra. Values in brackets were only used in the final combined calibration. For transitions from $n > 3$, only the strongest line was used in the calibration.

| Ion | Transition | Reference value (eV) | Residuals Ni campaign (meV) | Residuals Fe campaign (meV) |
|---|---|---|---|---|
| Fe XXV | 1$s$-2$s$ ($z$) | 6636.612[a] | 14(14)(295) | −35(11)(219) |
| Fe XXV | 1$s$-2p ($x$) | 6682.333[a] | −75(39)(280) | −14(28)(199) |
| Fe XXV | 1$s$-2$p$ ($w$) | 6700.434[a] | −17(22)(287) | 22(8)(206) |
| Fe XXVI | $Ly_{\alpha,2}$ | 6951.968[b] | [−35(170)(426)] | |
| Fe XXVI | $Ly_{\alpha,1}$ | 6973.182[b] | [63(84)(433)] | [461(211)(365)] |
| Ni XXVII | 1$s$-2$p$ ($w$) | 7805.605[a] | −58(24)(310) | |
| Fe XXV | 1$s$-3$p$ ($^3P^o$) | 7871.876[a] | [360(90)(308)] | [−20(51)(277)] |
| Fe XXV | 1$s$-3$p$ ($^1P^o$) | 7881.179[a] | 121(40)(308) | −35(28)(275) |
| Fe XXV | 1$s$-4$p$ | 8295.482[a] | −164(83)(452) | 117(128)(277) |
| Fe XXV | 1$s$-5$p$ | 8487.318[a] | [177(194)(616)] | [66(59)(351)] |

[a]Reference [11].
[b]Reference [29].

individual pixels and the time drift of the detector response. In a first step, we precalibrated the individual pixels for each individual measurement using a linear function and two strong He-like lines. For the Ni campaign we chose Fe w and Ni w, and for the iron measurements Fe w and He-like Fe $K_{\beta,1}$. This precalibration, performed for each measurement, corrects for discrete changes in the detector response between them. We then combined all the measurements for each individual pixel in the respective campaign, leaving us with one spectrum per pixel. This combined spectrum is then calibrated using a third-degree polynomial and additional calibration lines, as presented in Table I. We then add the spectra of all pixels to produce one spectrum per campaign.

The signal in this summed spectrum is about a factor of 30 higher than that of a single pixel. We exploit this to perform a more precise time-drift correction. In the combined spectrum, we observe how the centroids of the strong lines used for the initial linear calibration evolve over time. This enables us to correct for time drifts common to all pixels, which we found to dominate over pixel-to-pixel variation. Any remaining drifts of single pixels may still broaden the spectrum, but correcting the combined spectrum prevents a systematic offset of the spectral lines in the total spectrum.

To achieve this, we track the energy centroids of the two strongest calibration lines over time by dividing the data into time sections and fitting the line positions in each. We then define a linear correction for the energy for each section to keep the two lines at their reference values, and interpolate between sections to correct each recorded event. This compensates for short-term drifts within one measurement, whereas jumps between measurements were already accounted for in the initial correction step. Figure 1 shows an example of this procedure for the first measurement in the Ni campaign. We find that applying this correction also improves the temporal stability not only for the He-like lines used for the tracking but also for the other lines in the spectra, confirming its value. This is illustrated in the lower panel of the figure, where the improved stability of the Fe XXV $K_\beta$ line is demonstrated, which was not used for the time drift correction in the Ni campaign. We also inverted the order of the correction steps by starting out with the temporal correction of the single-pixel spectra. However, due to much lower statistics, this approach yielded broader spectral lines and larger remaining drifts in the combined spectrum. Therefore, we opted for the order of correction steps explained above and corrected the time drift in the summed spectrum.

To estimate the common systematic uncertainty introduced by this procedure, we recalibrated the time-corrected summed spectrum in a final step, taking into account all events across the entire campaign. With improved statistics compared to the single-pixel case, we could add calibration lines that had been too weak to fit in the single-pixel spectra. The results are shown in Fig. 2, where a second-degree polynomial was used for the dispersion curve fit. As the calibrated range was extended in this summed-spectrum-calibration step the second-order polynomial is the lowest order which can be employed here, considering the nonlinearity of the detector. In our previous work [30] we could employ a linear function for this purpose, as the calibrated energy range was not increased in the summed-spectrum calibration.

Apart from the common systematic uncertainty, the calibrations of the individual pixels increase the total systematic uncertainty. After taking into account the common residuals of the summed spectrum, the misalignment between individual pixels $i$ can be assumed to be independent from each other. We quantify this by calculating the mean confidence band, defined as $\bar{\sigma}_i(E) = \sum_i^N \frac{\sigma_i(E)}{N}$ with $\sigma_i(E)$ being the $1\sigma$-confidence band of the individual pixel $i$, and dividing by the square root of the number of pixels used, $N$:

$$\sigma_{\text{sys}}^{\text{individual}}(E) = \frac{1}{\sqrt{N}} \sum_i^N \frac{\sigma_i(E)}{N}. \tag{1}$$

This estimate assumes that the remaining pixel-level calibration deviations are statistically independent after the common calibration residual contribution has been treated separately. The uncertainty given by a deviation of the combined spectrum from the assumed calibration curve was already taken into account by the common residuals in the summed spectrum. The uncertainties of the chosen reference lines as given in [11,29] are negligibly small. The confidence bands discussed here are the result of the covariance of the polynomial fits, with the statistical uncertainty of the line centroid determination of the calibration lines taken into account.

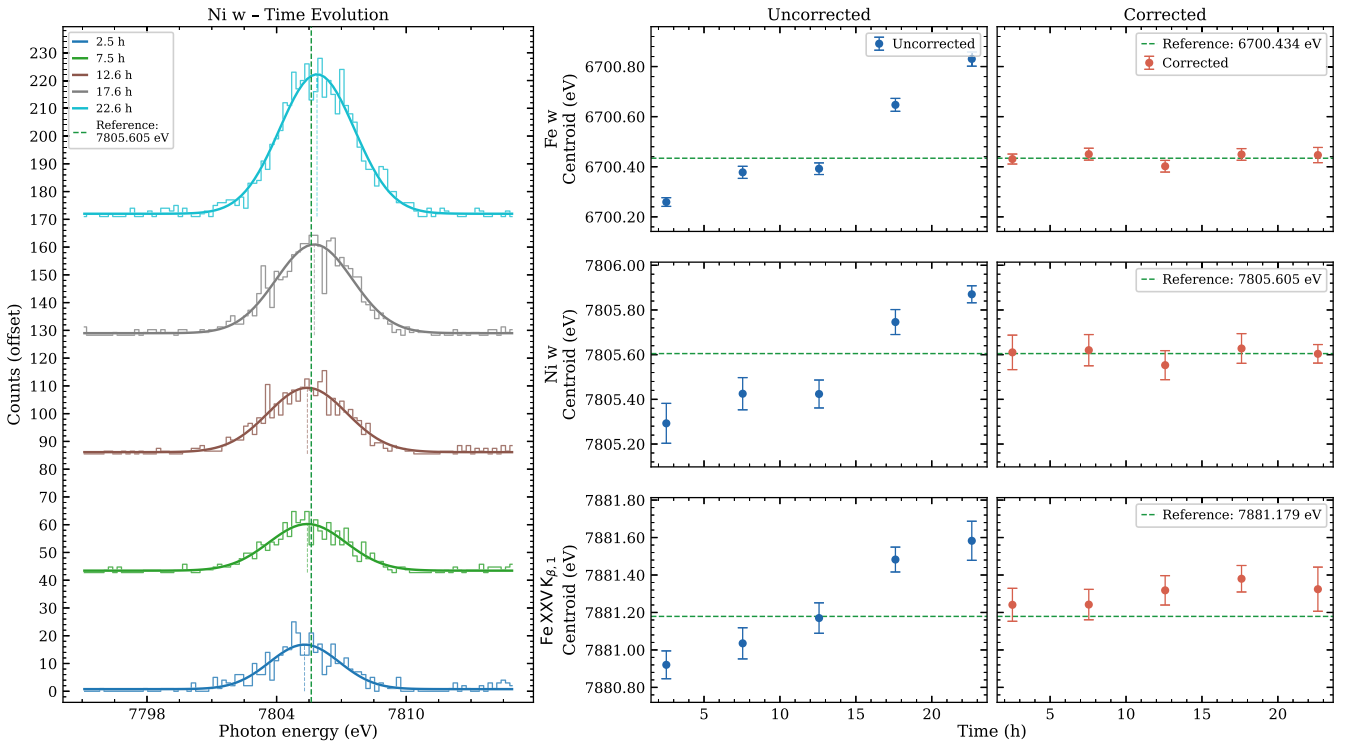



FIG. 1. Combined spectral time-drift correction for the first measurement of the Ni campaign. Left: Fits to the Ni w line for each of the five time slices following the drift of its centroid before the time-drift correction. The observed count rate increase of the Ni-w line over time is the result of a continuous shift of the ion content in the trap from iron to nickel after switching to nickel injection in this measurement. Right: Positions of the line centroids over time before and after the time-drift correction. The two lines at the top are used for the correction. For correcting the third line, Fe XXV $K_{\beta,1}$, we extrapolate the results of the other two as described in the main text.

After performing the described time-drift correction, we estimated the influence of the residual temporal drift of the energy response on our transition energies by fitting each spectral line in the final spectrum twice: once for the first half of the measurement campaign and once for the second. This quantifies any monotonous shift of the line centroids during the respective campaign. Such monotonous shifts would be most problematic in the presented data, as the calibration data was taken primarily at the beginning of the two campaigns. A monotonous shift would then lead to a systematic offset

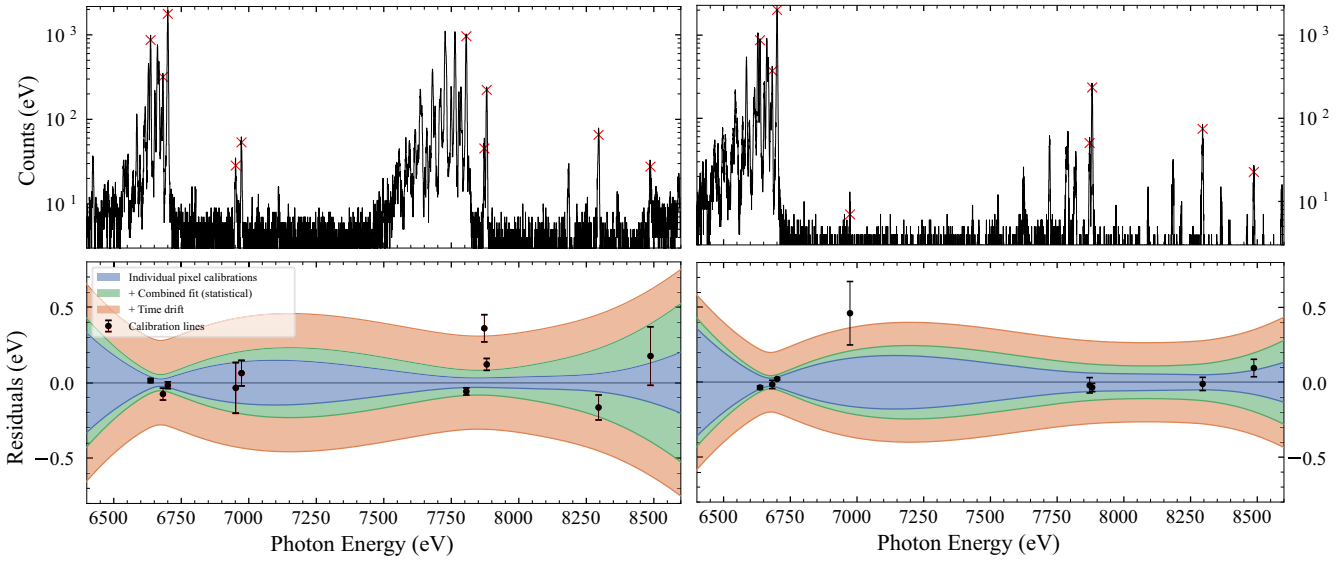



FIG. 2. Calibration of the sum spectra for the Ni (left) and Fe campaigns (right) with a quadratic function. In the top panels, calibration points are marked with crosses. Bottom panels show their residuals, with systematic uncertainty bands stacked. Corresponding literature values and residuals are listed in Table I.

between the calibration lines and the lines of interest. Higher order shifts do not cause a systematic offset to the calibration lines, but rather broaden the spectra. This effect may increase the statistical fit uncertainties but does not constitute an additional independent uncertainty component. Since sufficient statistics and the presence of the lines in both time slices are needed, we compared only the stronger, persistent transitions. For Ni, this was possible for all transitions with energies between 7600 eV and 7805 eV. We found an average energy deviation of 230 meV. For all Be-like to He-like transitions in our Fe data, the average deviation was 155 meV. These deviations are larger than the average statistical uncertainty. This remaining drift is due to nonlinearities in the time drift of the detector not corrected for by our correction algorithm. A correction matrix $c(i, t, E)$ that more accurately models the TES behavior requires more well-known strong fiducial lines for tracking purposes.

To account for the uncertainty introduced by this residual time drift, we add its contribution to the systematic uncertainty of all transition energies, and sum all three discussed error sources in our systematic uncertainty estimates. This systematic uncertainty estimate constitutes a conservative estimate rather than a strictly defined standard deviation.

Figure 2 shows the calibration of the summed spectra with marked calibration lines for the quadratic recalibration of the combined and corrected spectra with residuals and systematic uncertainty bands. All statistical uncertainties are 1-$\sigma$ fit uncertainties. All systematic uncertainties are obtained by the three-part uncertainty budget discussed above. The calibration lines used, their reference values and residuals after the calibration, and corresponding statistical and systematic uncertainties are listed in Table I. Lines, which were only used for the final recalibration of the sum spectra and not for the calibration of the individual pixels, are given in square brackets.

### B. Simulations

We compare the experimental data to spectra simulated with the collisional radiative model (CRM) of the Flexible Atomic Code (FAC) [31]. As input for the electron energy in the simulation we assume a Gaussian distribution centered on our nominal value of 11 000 eV with a width of 35 eV for the Ni and 9500 eV for the Fe measurements, respectively. The width was estimated based on radiative recombination lines from measurements at similar currents and trap parameters. We estimated the electron density to be $10^{12}\,\mathrm{cm}^{-3}$. Varying both parameters around the adopted values did not substantially alter the intensity ratios in the simulated spectra.

Spectra down to Ni XX and Fe XVIII were simulated with each calculation containing states with a principal quantum number of up to $n = 4$ for the F-like and up to $n = 6$ for He-like ions. To compare with the experimental results, the simulated spectrum of each charge state was shifted by a constant energy to match the strongest observed $K_\alpha$ transition of the respective charge state. These empirical shifts accounted for uncertainties in the calculated ground-state energy, ranging from 1.3 eV for Ni XXVII and 3.3 eV for Ni XX and similarly between 0.6 eV for Fe XXV and 3.5 eV for Fe XXI.

Furthermore, to account for the unknown charge-state distribution in the trap, the intensities of the simulated spectra were scaled so that the intensities of the strongest emission line of each charge state matched those observed experimentally. The shifted and normalized simulated spectra are overlaid on the experimental spectra in Figs. 3 and 4 for the nickel and iron data, respectively. Accordingly, the FAC spectra are used here to guide line identification and blend assignment; the shift-and-scale procedure is not intended as an absolute prediction of transition energies or charge-state populations.

In an additional set of calculations, we use many-body perturbation theory (MBPT), (see, e.g., [32–34]) combined with configuration interaction (CI) as implemented in FAC. We find that they agree better with the experimental results. Our empirical energy shifts to account for the uncertainty in the ground-state energy were between below 1 eV for all ions, much smaller than for the pure-CI calculations. However, due to their computational cost, we could not apply MBPT to some transitions originating from metastable states and high-$n$ levels. Comparisons of both methods and the experiments are presented in the Appendix B. Both sets of calculations include QED effects as given by the default settings in FAC, including vacuum polarization and electron self-energy, as well as the normal and specific mass shift. For the $K$-shell emissions in iron the mass shifts, as calculated by FAC, are on the order of 50–100 meV.

### C. Transition energies and line identification

We extracted the line centroid energies from our experimental spectra by fitting sums of Gaussians using maximum-likelihood fitting with Cash statistics [35]. For practical reasons, we divided the spectrum into several fit regions and modeled in each of them a background due to unresolved weak transitions using a linear function with offset and slope as free parameters. All fits performed to extract transition energies are shown in the Appendix B in Figs. 8–10.

We estimated the number of lines in each region by comparing our experimental spectra and simulations. The line centroids and amplitudes were treated as free parameters in the fits, with initial estimates taken from the simulations. The line widths are assumed to be the same within each individually fitted region. We allowed the width to vary slightly between regions due to energy-dependent detector resolution and pixel alignment. For the Ni measurements, the resolution (full width at half maximum, FWHM) was between 3.5 eV at 6.6 keV and 5.5 eV at 8.5 keV, for Fe between 3.4 eV at 6.6 keV and 4.2 eV at 8.5 keV. The better resolution during the Fe measurements was due to a higher stability of the cryostat of the microcalorimeter during those measurements. In future, better alignment of the pixels and correction of the temporal drift would enable achieving the resolution at the single-pixel level of 2 eV at 5.9 keV found during commissioning of the detector with an Fe-55 source. For this purpose, we just developed a solid-target fluorescence source producing strong fiducial lines. In any case, the accuracy of the transition energies determined in this study is limited by systematic uncertainties introduced by the calibration and not by statistics.

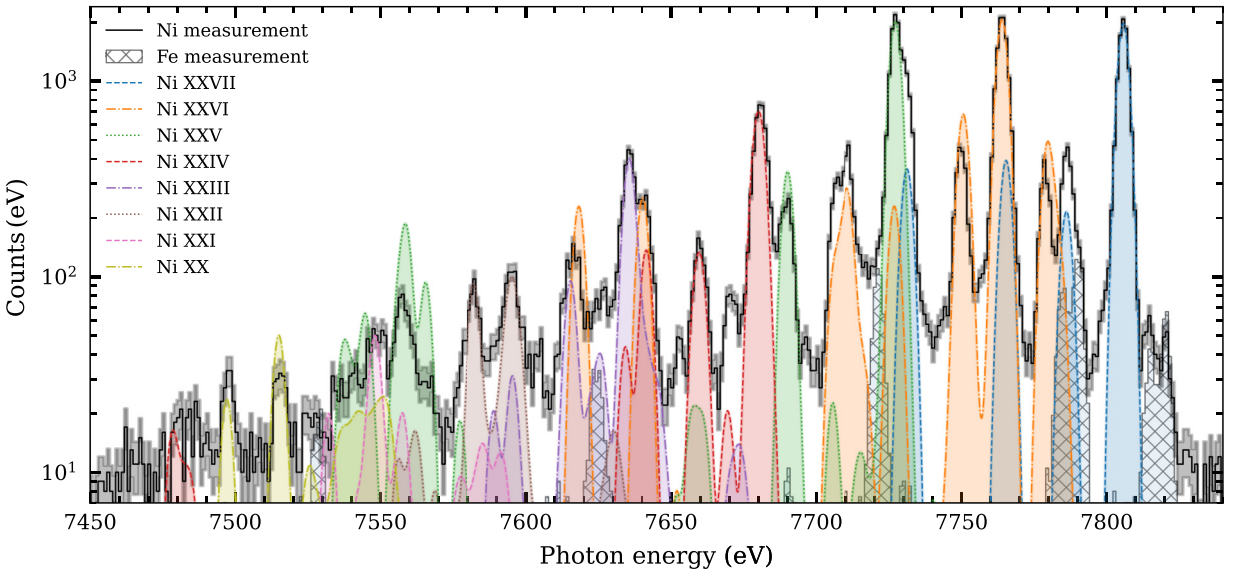



FIG. 3. Measured $K_\alpha$ spectrum of highly charged Ni ions compared to our FAC CRM calculations from Ni XXVII to Ni XX. The calculated spectra of each charge state are shifted by a constant energy and have their intensity rescaled to match the experiment. The measured iron spectrum, scaled to the Fe XXV-$K_\beta$ lines observed in the Ni measurement is overlaid as a gray hatched area.

To identify the fitted transitions we search around the fit results for the line centroids of each fitted Gaussian. In cases where several transitions significantly contribute to a fitted line, we list the major ones and mark the stated transition energy as belonging to a line blend. The final transition energies for all identified transitions are listed in the Appendix B in Tables II–V and shown in Figs. 8–10 with blends marked by angled brackets with the major transitions contributing to the blend listed. We list the literature values as collected in ATOMDB and NIST ASD [36] there for comparison. In the case of Fe, we also compare to previous experimental results from synchrotron measurements from [15,16,18]. Our Ni transition energies are also compared to tokamak measurements performed in [9]. To identify contributions from the $K_\beta$ emissions of residual Fe ions in the trap during the Ni measurement, we normalize the simulated Fe spectra to the stronger Fe-$K_\alpha$ emissions we observe in our spectrum. We confirm this normalization with the intensity of the Fe XXV $K_\beta$ emissions at 7871 eV and 7881 eV, and find only negligible contamination.

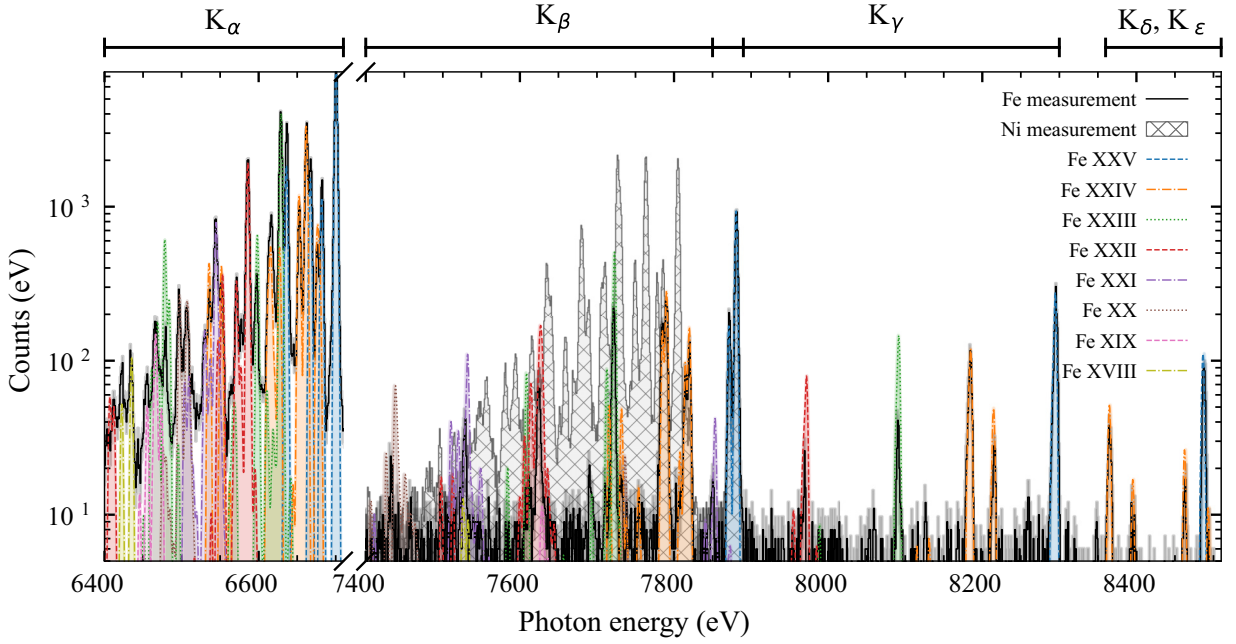



FIG. 4. Results of our Fe measurements and FAC CRM calculations from Fe XXV to Fe XVIII. The calculated spectra of each charge state are shifted and have their intensity rescaled to match the experiment. Left: $K_\alpha$ region. Right: $K_\beta$ to $K_\epsilon$. To illustrate the overlap with the Ni $K_\alpha$ region the measured nickel spectrum is overlaid as a gray hatched area.

Remaining deviations of the observed relative intensities from the simulations most likely result from uncertainties in the simulated line ratios. These are notoriously difficult to model, especially for charge states with more than two electrons and many possible pathways for excitation and radiative decay.

Based on our simulations, we expect significant blending between the transitions of the low charge states of nickel. In our transition energy tables, we mark the lines for which multiple transitions are expected to contribute significantly to the observed signal. In these cases, we provide the centroid of the blend as observed in our experiment. This centroid is subject to parameters influencing line ratios and charge state balance in the observed plasma, e.g., density and temperature. For these blended features, the quoted centroids are therefore dependent on the present EBIT excitation conditions.

Figure 4 shows the combined spectrum from the iron campaign with the $K_\alpha$ region on the left and the $n > 2$ transitions on the right. Using the simulated spectra, we identified the main $K_\beta$ emissions of Fe XXV to Fe XX in the spectrum. In the stronger $K_\alpha$ region we can identify lines down to Fe XVIII. Beyond the $K_\beta$ region we are also able to observe $K_\gamma$ emissions of Fe XXV to Fe XXI. $n > 4$ lines are only visible for Fe XXIV and Fe XXV.

Comparing our observed $K_\alpha$ transitions to synchrotron studies [15,16] shows good agreement within the experimental errors for most of the lines. Due to much higher resolution at the synchrotron and the more difficult calibration of the TES in this energy region the synchrotron results have a much lower uncertainty than the experimental data from the TES. A major difference between synchrotron studies and this experiment is the excitation mechanism. Here electron impact, at synchrotrons resonant photoexcitation. Thus, we can see transitions from states that are not easily accessible there. This is evident at the lower end of the $K_\alpha$ region, where more lines are seen than in synchrotron studies. Our resolution causes, therefore, more overlapping and makes it difficult to separate those blends. This explains differences in some of the line centroid energies between the two studies. We provide the centroid of the line blends, but we cannot establish a clear one-to-one correspondence between all transitions. Due to the greater separation of spectral lines at higher energies, line blending is less problematic for the $K_\beta$ lines and transitions from higher charge states. Considering this, our results for the iron $K_\beta$-transition energies agree well with those reported in [18].

We compare all isolated lines reported in this work to the values from [15,18] which have a much lower uncertainty. Lines used for calibration are excluded. We compare the differences of the values with their quadratically added total uncertainties. For 15/22 (68%) transition energies we find an agreement within the combined uncertainties. For 21/22 (96%) lines agreement is found within two times the combined uncertainty. These values are close to an ideal Gaussian distribution of values with correctly estimated uncertainties.

This strengthens confidence in our estimation of the uncertainty budget and the provided transition energy values for the lower charge states for which no precise data were available.

We note a periodic modulation of the residuals on the Fe w line in Fig. 9. We observe this effect only for this transition due its high statistics and the excellent alignment of the pixels at that energy, which make it ideal for calibration and time-drift correction. It is the result of the apparative line profile of the detector, which is not perfectly modeled by a single Gaussian but rather includes an additional low-energy tail. This is typical for TES as observed for example in [37,38]. Since we cannot reliably determine this profile and fit it in the single-pixel data due to low statistics, we choose to use single Gaussians in the calibration and subsequent analysis for all lines in the data. Since the calibration lines are also treated in this way, this does not introduce an additional systematic error. We also used a model with an additional, lower-energy, broader Gaussian at the low energy side of the transitions, and extracted the relative position, amplitude, and width from the Fe w line. Fixing these parameters for all other lines and applying this line shape in both the calibration and subsequent analysis did not change the results beyond the quoted uncertainties.

## IV. DISCUSSION AND CONCLUSION

With our combination of a TES array and an EBIT, we measured the transition energies of Ni $K_\alpha$ and Fe $K_\alpha$ up to $K_\delta$ for the charge states between He-like and F-like. For the Ni transitions we reached a median total uncertainty of 360 meV, corresponding to approximately 14 km/$s$, and for Fe, 340 meV, or 13 km/$s$, respectively. For this, we developed a correction and calibration procedure to provide accurate results in spite of TES nonlinearities and time drifts in this spectral region. By simultaneously observing nickel and iron and tracking the temporal drifts with two strong transitions, we substantially reduce uncertainties due to, e. g., instabilities of the cryogenic system. We quantify the systematic uncertainties conservatively as the linear sum of the individual pixel calibration uncertainty, summed spectrum residuals and average time shift of the individual lines across the two halves of the respective campaign. To suppress such residual calibration shifts in future studies, we have recently implemented a multi-element solid-target source generating characteristic fluorescence x rays during the EBIT measurements. These lines allow us to track detector drifts much more easily across the whole range of detectable photon energies, and will help lowering the systematic uncertainties even more in future studies.

By comparing our experimental results to spectra simulated with the FAC CRM module, we could identify the electronic configurations involved in all transitions.

While most of the $K_\alpha$ transitions of iron had already been studied using photoexcitation at higher resolution than in the present work [15,16], the $K_\beta$ and $K_\gamma$ transitions of this study have not been measured at high accuracy before. The overall good agreement of our results with the lines measured previously at the synchrotron increases our confidence in the determined transition energies for the formerly unmeasured lines.

We use the transition energy results from our extensive line study to compare our calculations done with pure CI and those including MBPT. This comparison is enabled by the low uncertainties for the transition energy centroids we achieved. In general, our MBPT calculations agree better

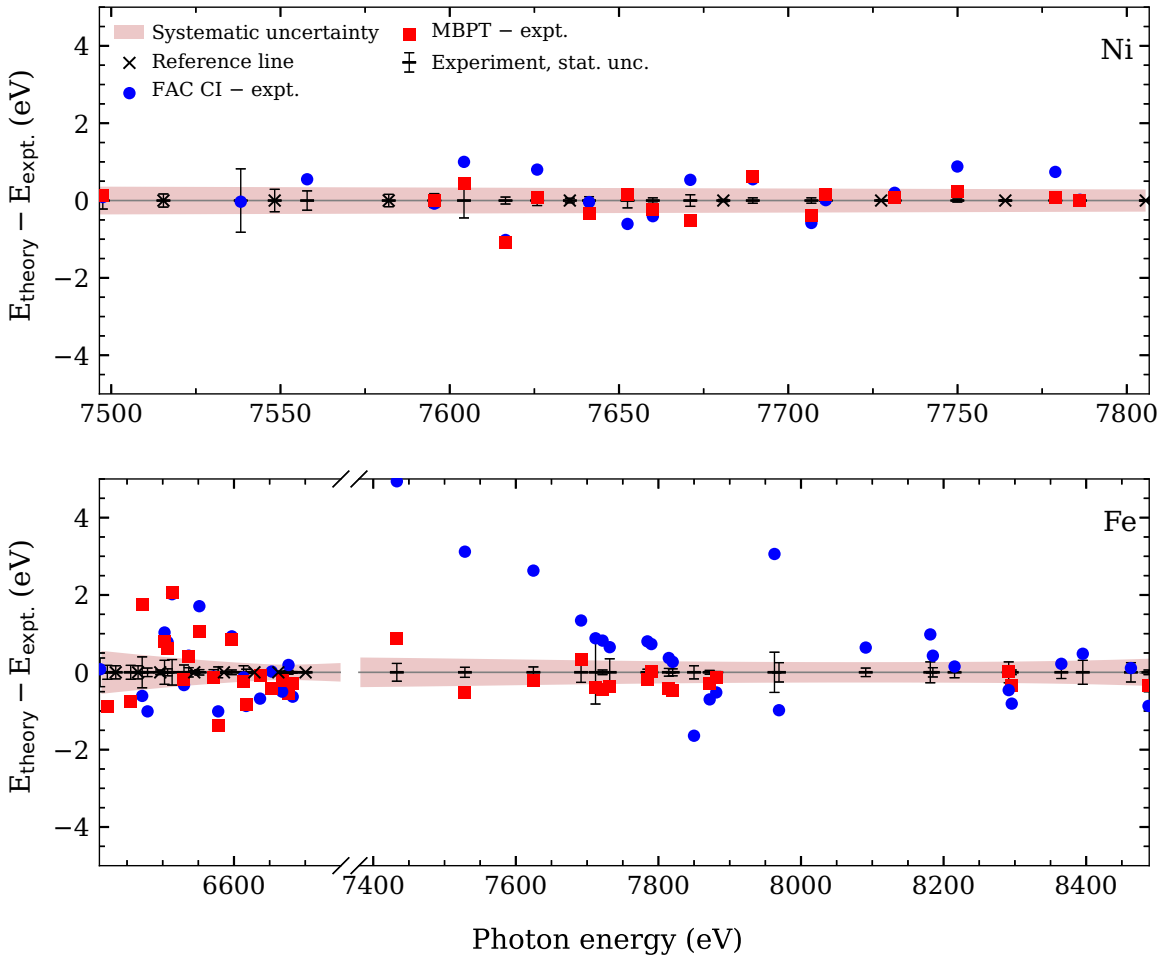



FIG. 5. Residuals between experimentally determined and calculated transition energies with pure CI (blue circles) and MBPT (red squares) for nickel (top) and iron (bottom). The red-shaded region marks the systematic uncertainty, and the error bars on the experimental energy markers denote their statistical uncertainties. Experimental transition energies marked with a cross are used as reference lines to fix the ground-state energy of the calculations and agree, therefore, by construction with the experiment. In cases of line blends, the energies of the contributing transitions is averaged.

with the experimental data than those made using only CI. The top panel of Fig. 5 shows the corresponding residuals for nickel and different calculations listed in Table II, where theoretical values attributed to a line blend are represented by the in CRM intensity weighted sum of blending transitions. Excluding the reference lines fixed to experimental values, we find that approximately 75% of the MBPT values agree with the experiment within the total uncertainty, which is determined by adding the statistical and systematic uncertainties in quadrature. This is close to the expected 68.3% $1\sigma$ coverage for an ideal Gaussian distribution. The pure-CI calculations agree only for 39% of the lines.

Similarly, for the $n \geqslant 3$ transitions in iron, as shown in the lower panel of Fig. 5, agreement is reached for 56% of the MBPT results but only for 12% of the pure CI calculations. For the low charge states in the iron $K_\alpha$ region, the agreement is worse, especially for the MBPT calculations. This can be attributed in part to the aforementioned line blending. While adding more configurations can improve the accuracy of CI calculations, it also increases computation time, and diminishes the advantage of faster computation times that those have with respect to MBPT models.

In both sets of calculations QED effects and mass shifts have been treated in the same manner, hence any difference in the performance of the calculations can be attributed directly to the addition of the MBPT. Although relativistic nuclear recoil contributions are included in the FAC calculations, a full QED treatment of the recoil terms was beyond the scope of the present work. The estimated contributions from these uncalculated QED recoil terms are however much smaller than the current uncertainty of the CI treatment on the present, limited-size basis set.

For the comparison of the calculation methods, studying intermediate charge states with more than two electrons is especially vital, as was done in this study. For these more complicated ions, the discrepancy between the different calculation methods is larger, and the benefit of including MBPT becomes clearer. This is also true when studying transitions involving upper states of higher $n$, particularly for these intermediate charge states, as is evident for the $K_\beta$ to $K_\delta$ transitions of iron observed here, where the MBPT calculations again outperform the pure CI calculations significantly.

Our present data will further directly help improving Ni and Fe abundance determinations carried out with

astrophysical codes such as SPEX and ATOMDB for a great variety of astrophysical objects. These results also provide urgently needed reference energies needed for benchmarking upcoming atomic structure calculations and plasma models in the critically important Ni $K_\alpha$−Fe $K_\beta$ spectral region.

## ACKNOWLEDGMENTS

The research leading to these results has received funding from the European Union's Horizon 2020 Program under the AHEAD2020 project (Grant Agreements No. 871158 and No. 654215). Research was funded by the Max-Planck-Gesellschaft (MPG), Germany. C.S. acknowledges support from MPG and NASA-JHU Cooperative Agreement.

## DATA AVAILABILITY

There are no publicly available research data or software supporting this manuscript. Requests for further information or data should be sent to the authors.

## APPENDIX A: DATA ANALYSIS PIPELINE DETAILS

Figure 6 shows the complete data analysis pipeline from the raw pulses to the final calibrated spectrum we analyze to extract the transition energies of iron and nickel.

To start out the data analysis, optimal filtering provides pulse-height estimates for each individual trace, as observed by the TES pixels. These pulse heights are then corrected for fluctuations of the baseline. The baseline is defined as the pretrigger mean of the pulse and contains useful information on the momentary behavior of the system, influenced, for example, by the temperature of the detector. We construct a running mean of the baseline in time and divide each pulse height by the ratio $\frac{B(t)}{B(t_0)}$ with $t_0$ being the starting time of the measurement campaign.

To provide additional details on the further data correction and calibration procedure, the next steps of the data analysis pipeline are detailed for the example of the nickel campaign and pixel 1. Figure 7 illustrates the effects of the individual correction and calibration steps described in the main text.

The individual-measurement, individual-pixel linear calibration, using two anchor points removes the large offsets between the measurements, as shown in Fig. 7(a). Summing the individual measurements prior to such a linear alignment causes the features to be broadened or split severly in the combined spectrum.

The nonlinearity in the energy-response of the detector is taken into account in the next step, in which the individual-pixel spectrum, consisting of all measurements of the campaign, in this example the three measurements of the Ni campaign, is calibrated with a cubic polynomial. The large residuals of the lines not used in the initial linear calibration get reduced from tens of eV to the sub-eV range, as depicted in Fig. 7(b). This is a result of the clearly nonlinear detector response.

After each pixel is calibrated with this cubic polynomial, their spectra are summed to obtain one spectrum for the complete campaign, as illustrated in Fig. 7(c). The good alignment of the individual spectra is illustrated by the stacked spectra in the figure.

Following the methodology described in the main text and shown in Fig. 1, the combined spectrum is subject to a finer time-drift correction. This finer correction was only possible in the combined spectrum due to the much higher statistics. Figure 7(d) shows again the time drift of the Ni w line before and after this step, reducing the drift from 0.6 eV to being compatible with the statistical errors of the fits to the individual time slices. This leads to the spectral lines in the time-integrated spectrum being narrower by the magnitude of the drift.

The last step is then the calibration of the time-corrected spectrum with the second-order polynomial as depicted in Fig. 2 in the main text. The $1\sigma$-confidence band of this calibration step lets us then determine the systematic uncertainty common to all pixels. As Fig. 7(e) shows, the effect of this step is subtle overall, mainly serving as a tool to estimate said common uncertainty component.

## APPENDIX B: ADDITIONAL TRANSITION-ENERGY TABLES AND FIGURES

This appendix presents detailed results for the observed iron and nickel transitions. Figures 8–10 show fits of sums of Gaussian components to the measured spectra. The reduced chi-squared value $\chi^2_\nu$ is given in each panel as an indication of the fit quality.

The fitted centroids are listed together with their transition or blend assignment in Tables II–V. Each experimental energy is reported with its statistical fit uncertainty and the combined systematic uncertainty from the three systematic contributions as defined in Sec. IIIA. The two uncertainties are given in brackets behind the experimental energies.

For each assigned transition, the measured energy is compared with the corresponding transition energy calculated using FAC in this work. Results obtained both with and without many-body perturbation theory (MBPT) are listed. Where available, previously published experimental or theoretical values are also included for comparison.

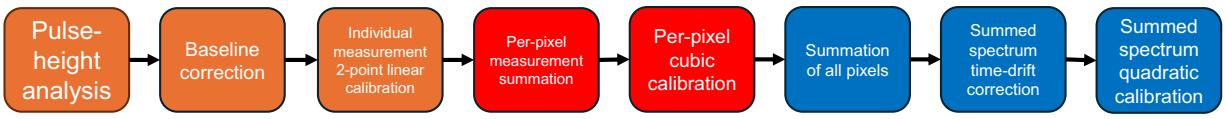



FIG. 6. Representative flow chart of the complete data analysis pipeline. Steps in orange color are performed on a single-pixel, single-measurement basis. Steps in red are performed on a combined-measurement, single-pixel basis. Steps in blue are performed on the complete spectrum of an entire measurement campaign. Details are provided in the main text.

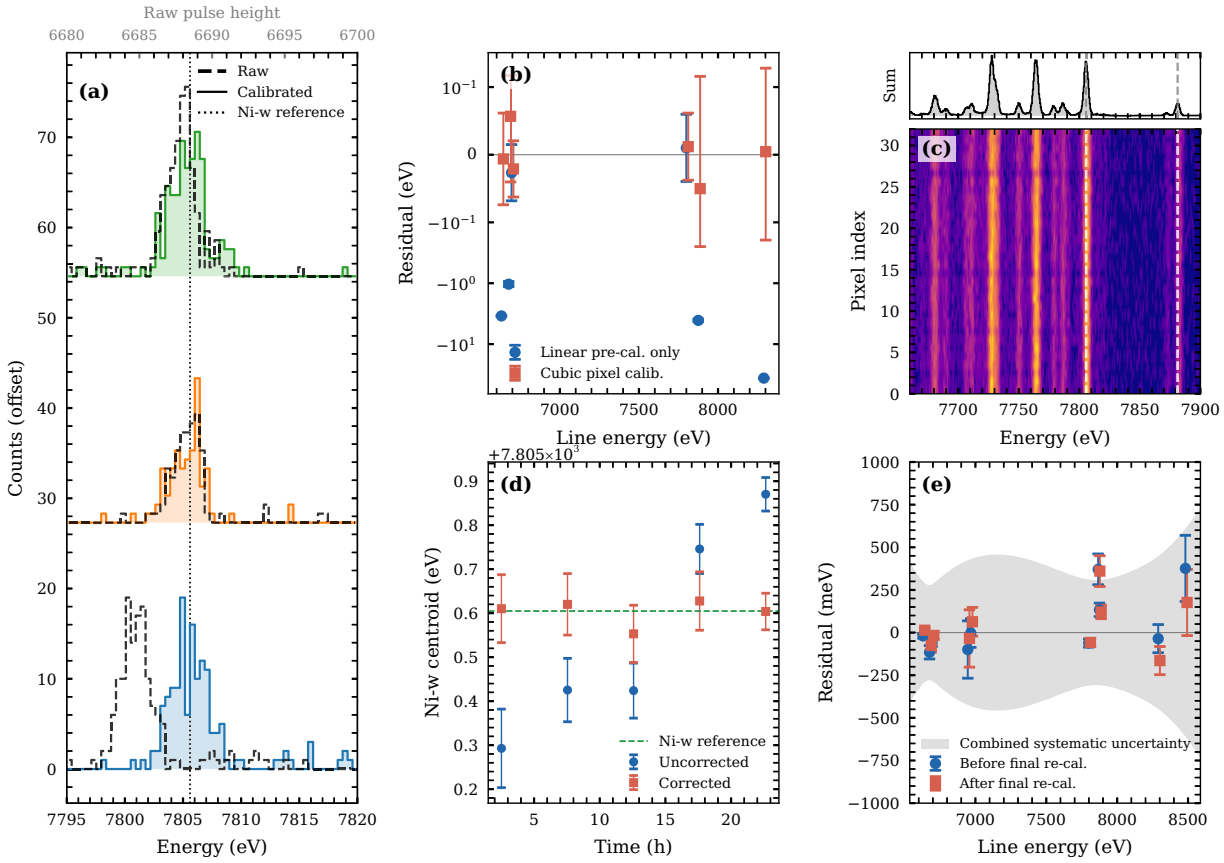



FIG. 7. Compact overview of the calibration pipeline for one representative pixel (Pixel 1, Ni campaign). (a) Raw (dashed, top axis) and linearly pre-calibrated (solid, bottom axis) spectra of the Ni-w line for the three submeasurements comprising this campaign, vertically offset for clarity; the linear precalibration removes the measurement-to-measurement offsets visible in the raw traces. (b) Residuals of the six calibration lines used in the single-pixel cubic calibration, comparing the linear pre-calibration alone (blue circles) to the full cubic polynomial calibration (red squares); error bars denote statistical centroid-fit uncertainties. Note the symmetric-log $y$ axis, required to display both the sub-0.1 eV residuals after the cubic calibration and the up to 36 eV residuals of the most distant line before it. (c) Calibrated spectra of all pixels as a function of pixel index (heatmap), with the summed one-dimensional spectrum shown above; vertical dotted lines mark the calibration lines. (d) Centroid of the Ni-w line as a function of time within Measurement I, before (blue) and after (red) the summed-spectrum time-drift correction, relative to the Ni-w literature value (green dashed line). (e) Residuals of all ten calibration lines used in the final recalibration of the time-corrected, summed spectrum, relative to their literature values, before (blue) and after (red) this final calibration step; error bars denote statistical uncertainties, and the gray shaded band shows the combined energy-dependent systematic uncertainty of the final calibration as discussed in the main text.

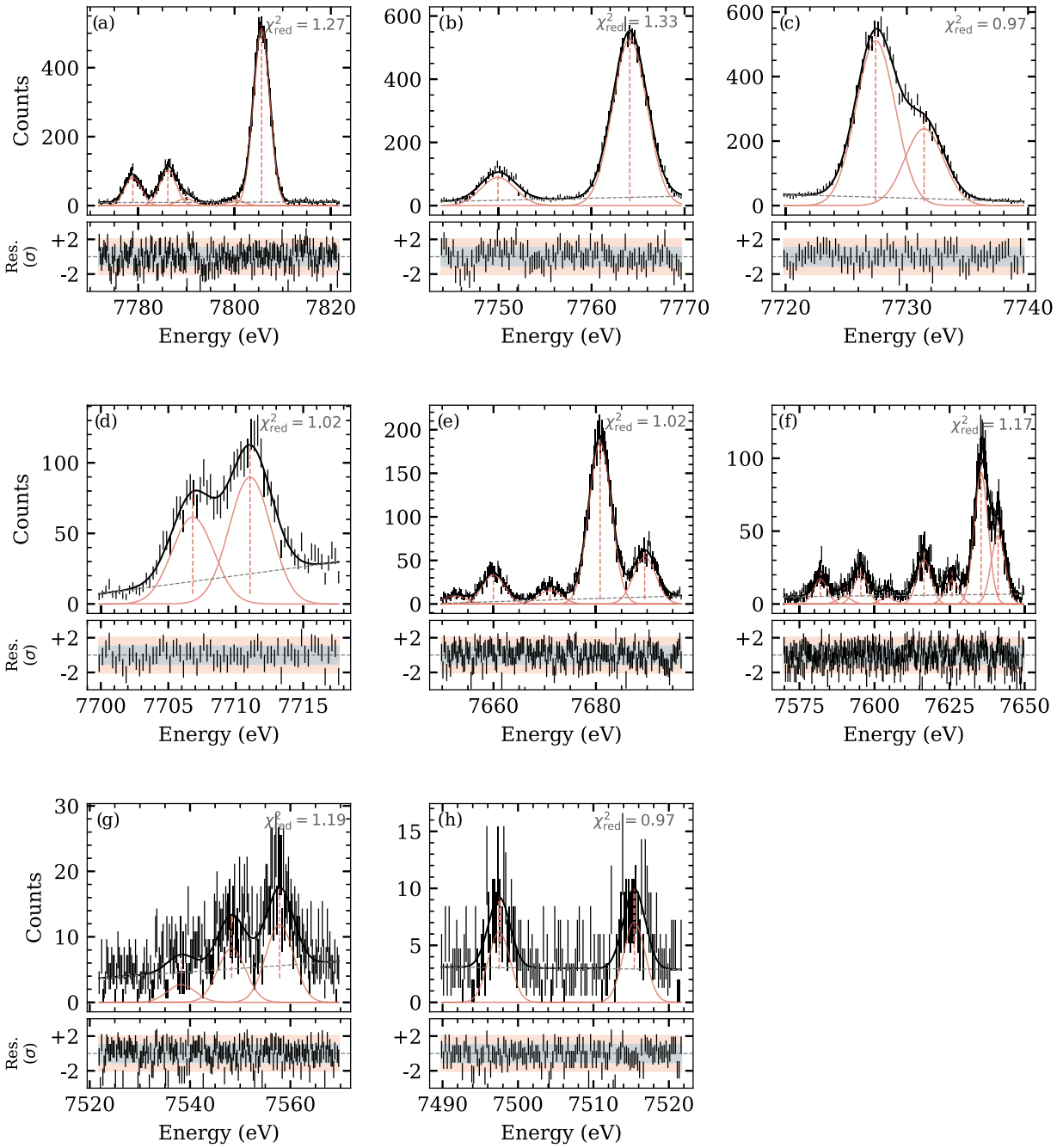



FIG. 8. All fits performed to the nickel data to extract the transition energies with corresponding fit residuals. Dashed lines mark the determined line centroids and the fitted linear background. The extracted transition energies are listed in Table II.

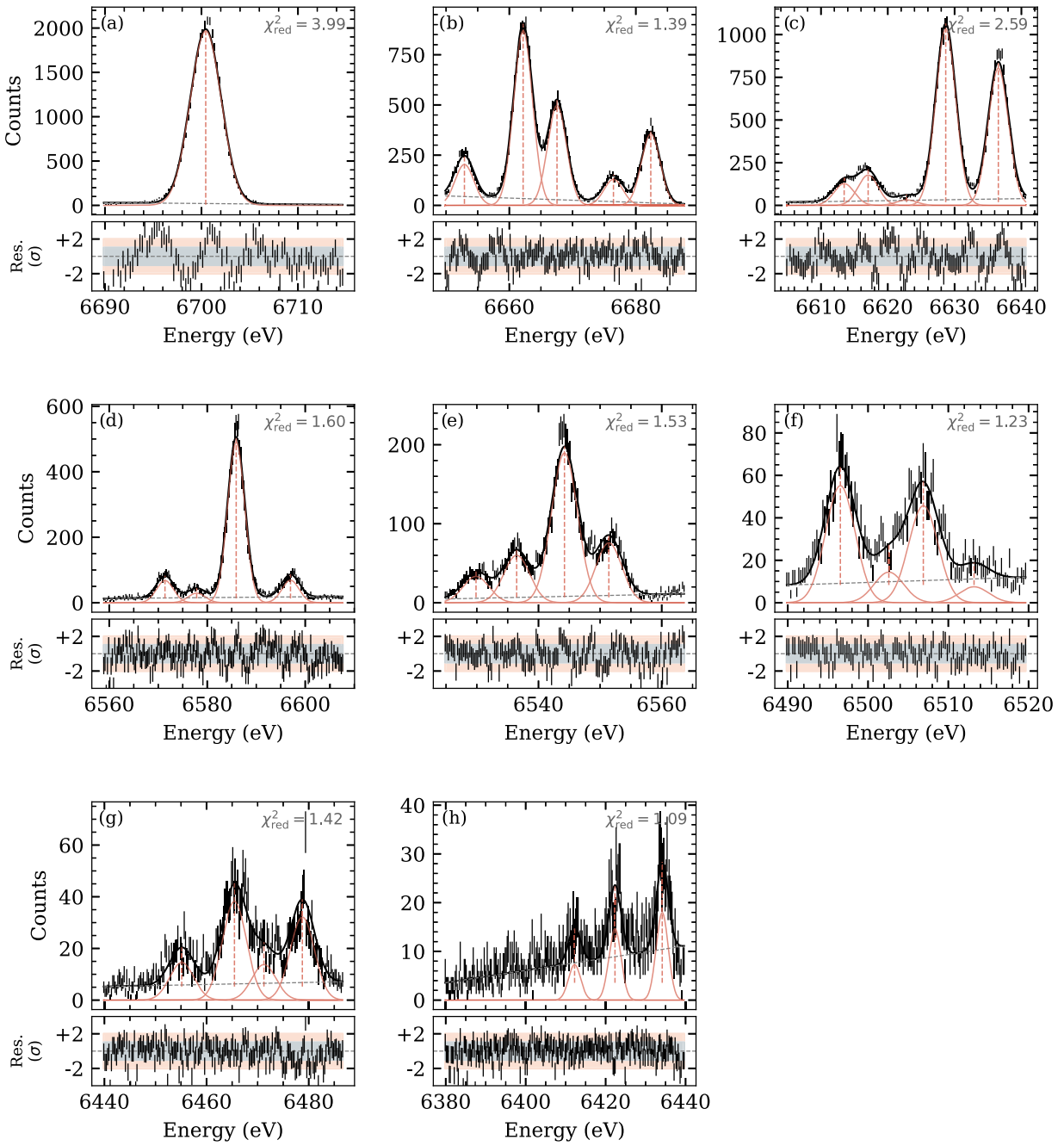



FIG. 9. Fits and residuals of the Fe $K_\alpha$ region used to extract the transition energies. Dashed lines mark the determined line centroids. The extracted transition energies are listed in Table III.

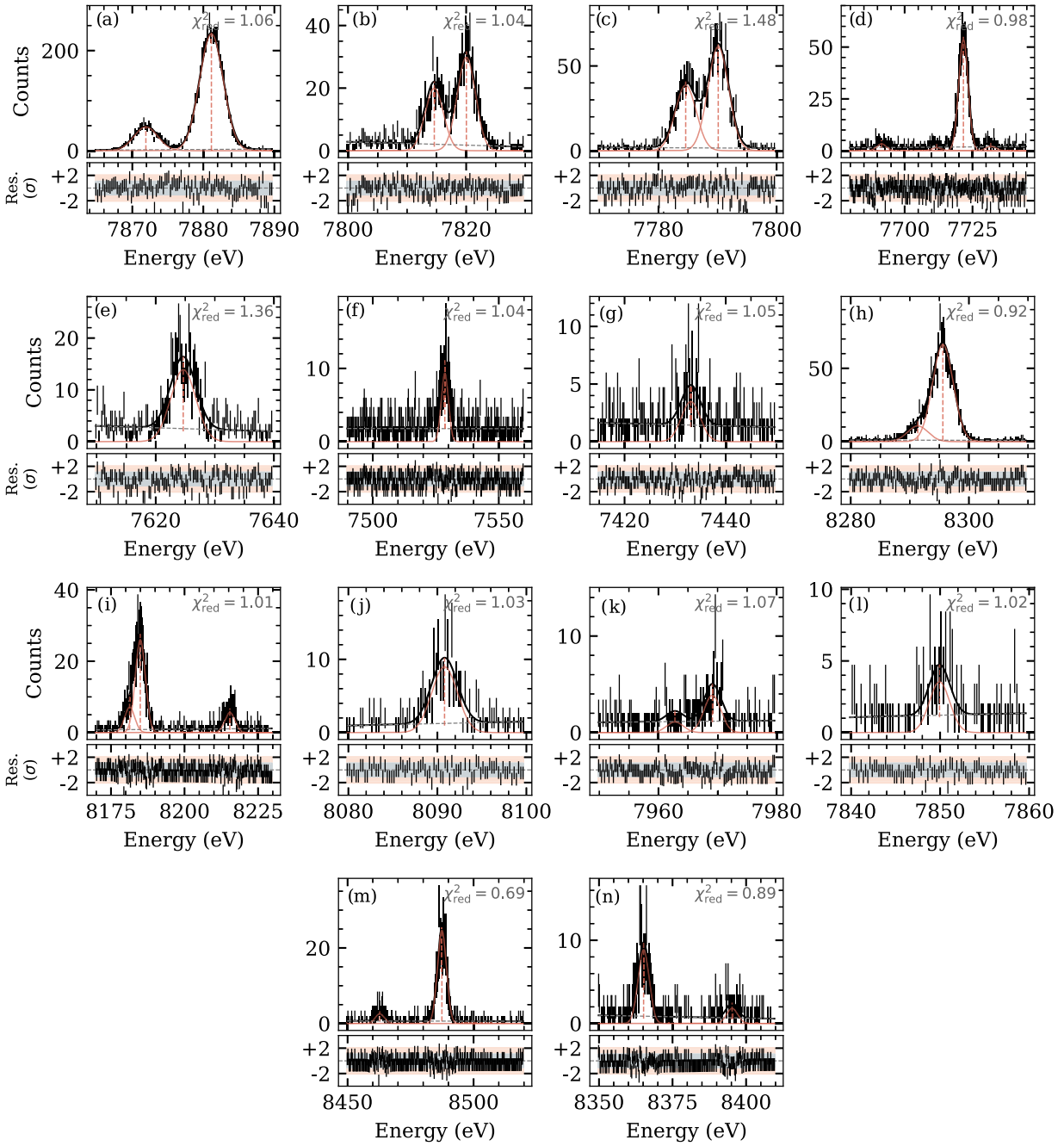



FIG. 10. Fits used to extract the Fe $n > 2$ -transition energies and their residuals. Dashed lines mark the determined line centroids and the fitted linear background. The results are listed in Tables IV and V.

TABLE II. Transition energies of all observed nickel emissions. The theoretical values in brackets are used to reference the ground-state energy of our calculations and thus agree by construction with the experiment. The experimental values in brackets are used in the calibration of the spectrum and thus agree by construction with the literature values. Configurations are given in *jj* coupling with full subshells omitted. The corresponding fits are shown in Fig. 8. Angled brackets denote line blends, which also contain the nearby transitions marked as (*).

| RoI | Ion | Lower state | Upper state | Transition energy (eV) | Theory (eV) (pure CI) | Theory (eV) (MBPT) | Literature |
|---|---|---|---|---|---|---|---|
| (a) | Ni XXVII | $[1s^2]_0$ | $[1s\,2p_{3/2}]_1$ | [7805.62(2)(31)] | [7805.62] | [7805.62] | 7805.605(1)[a]<br>7805(5)[b] |
| | Ni XXVII | $[1s^2]_0$ | $[1s\,2p_{3/2}]_2$ | 7786.15(6)(31) | 7786.17 | 7786.16 | 7786.424(1)[a] |
| | Ni XXVI | $[2s]_{1/2}$ | $[(1s\,2s)_1\,2p_{3/2}]_{1/2}$ | 7778.88(5)(31) | 7779.62 | 7778.97 | 7778.76(4)[c]<br>7778(5)[b] |
| (b) | Ni XXVI | $[2s]_{1/2}$ | $[(1s\,2s)_1\,2p_{3/2}]_{3/2}$ | 7764.11(2)(32) | [7764.11] | [7764.11] | 7763.67(4)[c]<br>7763(5)[b] |
| | Ni XXVI | $[2s]_{1/2}$ | $[(1s\,2s)_0\,2p_{1/2}]_{1/2}$ | 7749.94(4)(32) | 7750.82 | 7750.17 | 7750.12(4)[c]<br>7750(5)[b] |
| (c) | Ni XXVII | $[1s^2]_0$ | $[1s\,2s]_1$ | 7731.42(3)(32) | 7731.62 | 7731.49 | 7731.630(1)[a] |
| | Ni XXV | $[2s^2]_0$ | $[1s\,2p_{3/2}]_1$ | 7727.43(2)(32) | [7727.43] | [7727.43] | 7727(5)[b] |
| (d) | Ni XXVI | $[2s]_{1/2}$ | $[(1s\,2s)_1\,2p_{1/2}]_{3/2}$ | 7711.06(7)(33) | 7711.07 | 7711.22 | 7711.14(4)[c] |
| | Ni XXVI | $[2s]_{1/2}$ | $[(1s\,2s)_1\,2p_{1/2}]_{1/2}$ | 7706.82(7)(33) | 7706.24 | 7706.44 | 7706.36(4)[c] |
| (e) | Ni XXV | $[2s^2]_0$ | $[1s\,2p_{1/2}]_1$ | 7689.52(7)(33) | 7690.07 | 7690.13 | |
| | Ni XXIV | $[2p_{1/2}]_{1/2}$ | $[(1s\,2p_{1/2})_1\,2p_{3/2}]_{3/2}$ | 7680.81(3)(34) | [7680.81] | [7680.81] | 7680(5)[b] |
| | Ni XXIV | $[2p_{3/2}]_{3/2}$ | $[1s\,2p^2]_{5/2}$ | ⟨7671.06(15)(34)⟩ | 7669.29 | 7669.06 | 7669(5)[b] |
| | Ni XXIII | $[2p_{1/2}\,3s]_1$ | $\{[(1s\,2p_{1/2})_1\,2p_{3/2})_{1/2}\,3s\}_0$ | (*) | 7673.90 | 7672.02 | |
| | Ni XXIV | $[2p_{3/2}]_{3/2}$ | $[(1s\,2p_{1/2})_1\,2p_{3/2}]_{3/2}$ | ⟨7659.99(7)(34)⟩ | 7660.47 | 7660.47 | |
| | Ni XXIV | $[2p_{3/2}]_{3/2}$ | $[(1s\,2p_{1/2})_1\,2p_{3/2}]_{1/2}$ | (*) | 7658.70 | 7659.03 | |
| | Ni XXVI | $[2p_{3/2}]_{3/2}$ | $[(1s\,2s)_1\,2p_{3/2}]_{5/2}$ | ⟨7652.51(19)(35)⟩ | 7652.13 | 7652.43 | |
| | Ni XXV | $[2s\,2p_{3/2}]_2$ | $\{[(1s\,2s)_1\,2p_{1/2}]_{1/2}\,2p_{3/2}\}_2$ | (*) | 7651.68 | 7652.89 | |
| (f) | Ni XXVI | $[2p_{1/2}]_{1/2}$ | $[1s]_{1/2}$ | ⟨7641.15(10)(35)⟩ | 7640.41 | 7640.28 | 7640.35(4)[c] |
| | Ni XXIV | $[2p_{1/2}]_{1/2}$ | $[1s]_{1/2}$ | (*) | 7641.55 | 7641.13 | |
| | Ni XXIV | $[2p_{3/2}]_{3/2}$ | $[(1s\,2p_{1/2})_1\,2p_{3/2}]_{5/2}$ | (*) | 7641.37 | 7641.02 | |
| | Ni XXIII | $[2p^2]_0$ | $[1s\,2p_{3/2}]_1$ | 7635.48(6)(35) | [7635.48] | [7635.48] | |
| | Ni XXIII | $[2p_{1/2}\,2p_{3/2}]_1$ | $[(1s\,2p_{1/2})_0\,2p^2]_2$ | 7625.82(13)(35) | 7626.62 | 7625.90 | |
| | Ni XXIII | $[2p_{1/2}\,2p_{3/2}]_2$ | $[1s\,2p_{3/2}]_1$ | 7616.47(9)(36) | 7615.45 | 7615.38 | |
| | Ni XXIII | $[2p^2]_2$ | $[(1s\,2p_{1/2})_1\,2p^2]_3$ | 7604.21(45)(36) | 7605.21 | 7604.64 | |
| | Ni XXII | $[2p_{3/2}]_{3/2}$ | $[1s\,2p^2]_{3/2}$ | ⟨7595.44(18)(36)⟩ | 7594.79 | 7594.93 | |
| | Ni XXIII | $[2p_{3/2}]_{3/2}$ | $[1s\,2p^2]_{1/2}$ | (*) | 7595.93 | 7595.93 | |
| | Ni XXII | $[2p_{3/2}]_{3/2}$ | $[1s\,2p^2]_{5/2}$ | 7581.98(16)(37) | [7581.98] | [7581.98] | |
| (g) | Ni XXV | $[2p_{1/2}\,2p_{3/2}]_2$ | $[1s\,2p_{3/2}]_2$ | 7557.87(25)(38) | 7558.42 | | |
| | Ni XXI | $[2p^2]_2$ | $[1s\,2p^3]_2$ | 7548.29(29)(38) | [7548.29] | [7548.29] | |
| | Ni XXV | $[2p^2]_2$ | $[1s\,2p_{3/2}]_2$ | ⟨7538.26(82)(38)⟩ | 7536.77 | | |
| | Ni XXV | $[2p_{1/2}\,2p_{3/2}]_2$ | $[1s\,2p_{1/2}]_1$ | (*) | 7539.69 | | |
| (h) | Ni XX | $[2p^3]_{3/2}$ | $[1s]_{1/2}$ | 7515.42(17)(39) | [7515.42] | [7515.42] | |
| | Ni XX | $[2p_{1/2}]_{1/2}$ | $[1s]_{1/2}$ | 7497.51(22)(39) | 7497.60 | 7497.65 | |

[a]Reference [11] (Theory).
[b]Reference [9] (Experiment).
[c]References [12,39] (Theory).

TABLE III. Measured energies of the Fe $K_\alpha$ transitions. We show in brackets the theoretical values used as reference for the ground-state energy of our FAC calculations. The experimental values in brackets were used in the calibration of the spectrum and thus agree by construction with the literature values. The values from [18] in brackets are the centroids of the line complex. The corresponding fits are shown in Fig. 9. Angled brackets denote line blends, which also contain the nearby transitions marked as (*).

| RoI | Ion | Lower state | Upper state | Transition energy (eV) | Theory (eV) (pure CI) | Theory (eV) (MBPT) | Literature |
|---|---|---|---|---|---|---|---|
| (a) | Fe XXV | $[1s^2]_0$ | $[1s\,2p_{3/2}]_1$ | [6700.44(1)(21)] | [6700.44] | [6700.44] | 6700.434[a]<br>6700.549(5)(70)[b] |
| (b) | Fe XXV | $[1s^2]_0$ | $[1s\,2p_{3/2}]_2$ | [6682.36(2)(20)] | 6681.73 | 6682.06 | 6682.3333[a] |
| | Fe XXIV | $[2s]_{1/2}$ | $[(1s\,2s)_1\,2p_{3/2}]_{1/2}$ | 6676.46(5)(20) | 6676.65 | 6675.90 | 6676.202(3)(69)[b] |
| | Fe XXV | $[1s^2]_0$ | $[1s\,2p_{1/2}]_1$ | 6667.54(3)(20) | 6667.04 | 6667.33 | 6667.5780[a] |
| | Fe XXIV | $[2s]_{1/2}$ | $[(1s\,2s)_1\,2p_{3/2}]_{3/2}$ | 6662.18(2)(20) | [6662.18] | [6662.18] | 6662.240(6)(69)[b] |
| | Fe XXIV | $[2s]_{1/2}$ | $[(1s\,2s)_0\,2p_{1/2}]_{1/2}$ | 6652.90(3)(21) | 6652.92 | 6652.49 | 6652.826(3)(69)[b] |
| (c) | Fe XXV | $[1s^2]_0$ | $[1s\,2s]_1$ | [6636.55(1)(22)] | 6635.87 | 6636.46 | 6636.612[a] |
| | Fe XXIII | $[2s^2]_0$ | $[1s\,2p_{3/2}]_1$ | 6628.67(2)(23) | [6628.67] | [6628.67] | 6628.804(5)(68)[b] |
| | Fe XXIV | $[2s]_{1/2}$ | $[(1s\,2s)_1\,2p_{1/2}]_{3/2}$ | 6617.06(8)(24) | 6616.19 | 6616.24 | 6616.629(4)(68)[b] |
| | Fe XXIV | $[2s]_{1/2}$ | $[(1s\,2s)_1\,2p_{1/2}]_{1/2}$ | ⟨6613.47(17)(24)⟩ | 6612.44 | 6612.54 | |
| | Fe XXIV | $[2p_{3/2}]_{3/2}$ | $[(1s\,2p_{1/2})_0\,2p_{3/2}]_{3/2}$ | (*) | 6614.24 | 6613.94 | |
| (d) | Fe XXIII | $[2s^2]_0$ | $[1s\,2p_{1/2}]_1$ | 6596.99(6)(26) | 6597.92 | 6597.84 | 6597.858(3)(67)[b] |
| | Fe XXII | $[2p_{1/2}]_{1/2}$ | $[(1s\,2p_{1/2})_1\,2p_{3/2}]_{3/2}$ | ⟨6585.91(2)(28)⟩ | [6586.21] | [6586.03] | 6586.085(7)(67)[b] |
| | Fe XXII | $[2p_{1/2}]_{1/2}$ | $[(1s\,2p_{1/2})_1\,2p_{3/2}]_{1/2}$ | (*) | [6585.61] | [6585.79] | |
| | Fe XXII | $[2p_{3/2}]_{3/2}$ | $[1s\,2p^2]_{5/2}$ | 6577.84(14)(29) | 6576.83 | 6576.47 | |
| | Fe XXII | $[2p_{3/2}]_{3/2}$ | $[(1s\,2p_{1/2})_1\,2p_{3/2}]_{1/2}$ | ⟨6571.37(7)(29)⟩ | 6570.94 | 6571.11 | |
| | Fe XXII | $[2p_{3/2}]_{3/2}$ | $[(1s\,2p_{1/2})_1\,2p_{3/2}]_{3/2}$ | (*) | 6571.58 | 6571.35 | |
| (e) | Fe XXII | $[2p_{1/2}]_{1/2}$ | $[1s]_{1/2}$ | ⟨6551.42(7)(32)⟩ | 6553.21 | 6552.56 | |
| | Fe XXII | $[2p_{3/2}]_{3/2}$ | $[(1s\,2p_{1/2})_1\,2p_{3/2}]_{5/2}$ | (*) | 6553.05 | 6552.38 | |
| | Fe XXI | $[2p^2]_0$ | $[1s\,2p_{3/2}]_1$ | 6544.22(4)(33) | [6544.22] | [6544.22] | 6544.225(4)(66)[b] |
| | Fe XXI | $[2p_{1/2}\,2p_{3/2}]_1$ | $[(1s\,2p_{1/2})_0\,2p^2]_2$ | 6536.46(12)(34) | 6536.89 | 6536.86 | |
| | Fe XXI | $[2p_{1/2}\,2p_{3/2}]_2$ | $[1s\,2p_{3/2}]_1$ | 6529.87(19)(35) | 6529.54 | 6529.68 | |
| (f) | Fe XXI | $[2p^2]_2$ | $[1s\,2p_{3/2}]_1$ | ⟨6513.21(33)(38)⟩ | 6513.62 | 6513.82 | |
| | Fe XXII | $[(2s\,2p_{1/2})_1\,2p_{3/2}]_{5/2}$ | $[(1s\,2s)_1\,2p_{3/2}]_{5/2}$ | (*) | 6516.39 | 6516.38 | |
| | Fe XXI | $[2p^2]_2$ | $[(1s\,2p_{1/2})_0\,2p^2]_2$ | (*) | 6515.68 | 6515.65 | |
| | Fe XX | $[2p_{3/2}]_{3/2}$ | $[(1s\,2p_{1/2})_0\,2p^3]_{3/2}$ | ⟨6506.89(9)(39)⟩ | 6506.26 | 6506.28 | 6506.845(7)(65)[b] |
| | Fe XXI | $[2p_{1/2}\,2p_{3/2}]_1$ | $[1s\,2p_{3/2}]_2$ | (*) | 6509.08 | 6508.75 | |
| | Fe XXI | $[2p_{1/2}\,2p_{3/2}]_2$ | $[1s\,2p_{3/2}]_2$ | 6502.59(31)(40) | 6503.62 | 6503.39 | |
| | Fe XX | $[2p_{3/2}]_{3/2}$ | $[1s\,2p^2]_{5/2}$ | 6496.55(6)(41) | [6496.55] | [6496.55] | 6497.067(5)(65)[b] |
| (g) | Fe XXIII | $[2p_{1/2}\,2p_{3/2}]_2$ | $[1s\,2p_{3/2}]_2$ | ⟨6478.75(11)(44)⟩ | 6477.74 | | |
| | Fe XXIII | $[2p_{1/2}\,2p_{3/2}]_1$ | $[1s\,2p_{1/2}]_0$ | ⟨6471.23(40)(45)⟩ | 6468.37 | | |
| | Fe XIX | $[2p^2]_2$ | $[1s\,2p^3]_1$ | (*) | 6472.87 | 6472.99 | |
| | Fe XIX | $[2p^2]_2$ | $[1s\,2p^3]_2$ | ⟨6465.46(17)(46)⟩ | [6465.46] | [6465.46] | 6466.900(14)(64)[b] |
| | Fe XIX | $[2p_{1/2}\,2p^3]_1$ | $[1s\,2p^3]_2$ | ⟨6455.14(18)(48)⟩ | 6454.39 | 6454.38 | |
| (h) | Fe XVIII | $[2p^3]_{3/2}$ | $[1s]_{1/2}$ | 6434.16(17)(52) | [6434.16] | [6434.16] | 6435.239(14)(63)[b] |
| | Fe XVIII | $[2p_{1/2}]_{1/2}$ | $[1s]_{1/2}$ | 6422.34(18)(54) | 6421.45 | 6421.45 | |
| | Fe XXII | $[2p_{3/2}]_{3/2}$ | $[(1s\,2p_{1/2})_1\,2p_{3/2}]_{5/2}$ | 6412.23(37)(56) | 6412.31 | | |

[a]Reference [11] (Theory).
[b]Reference [15] (Experiment).

TABLE IV. Measured energies of the Fe $K_\beta$ transitions. Experimental values in square brackets are used for calibration and set to literature values. The values from [18] in brackets are averaged as centroids of the corresponding line complex similar to the fits shown in Fig. 10. Angled brackets denote line blends with the nearby transitions marked with (*).

| RoI | Ion | Lower state | Upper state | Transition energy (eV) | Theory (eV) (pure CI) | Theory (eV) (MBPT) | Literature |
|---|---|---|---|---|---|---|---|
| (a) | Fe XXV | $[1s^2]_0$ | $[1s\,3p_{3/2}]_1$ | [7881.14(2)(28)] | 7880.62 | 7881.00 | 7881.179(8)[a]<br>7882[b]<br>7881.37(1)(10)[c]<br>7880.67(15)[d] |
| | Fe XXV | $[1s^2]_0$ | $[1s\,3p_{1/2}]_1$ | [7871.91(5)(28)] | 7871.21 | 7871.61 | 7871.876(8)[a]<br>7872[b]<br>7871.88(7)(10)[c]<br>7871.31(25)[d] |
| (b) | Fe XXIV | $[2s]_{1/2}$ | $[(1s\,2s)_0\,3p_{3/2}]_{3/2}$ | 7820.03(9)(28) | 7820.30 | 7819.57 | 7820[b]<br>7820.15(16)(10)[c]<br>7819.88(20)[d] |
| | Fe XXIV | $[2s]_{1/2}$ | $[(1s\,2s)_0\,3p_{1/2}]_{1/2}$ | 7814.60(10)(29) | 7814.97 | 7814.18 | 7814[b]<br>7814.78(11)(13)[c]<br>7813.47(25)[d] |
| (c) | Fe XXIV | $[2s]_{1/2}$ | $[(1s\,2s)_1\,3p_{3/2}]_{3/2}$ | ⟨7790.12(5)(29)⟩ | 7790.63 | 7789.86 | 7790[b] |
| | Fe XXIV | $[2s]_{1/2}$ | $[(1s\,2s)_1\,3p_{3/2}]_{1/2}$ | (*) | 7791.07 | 7790.40 | ⟨7790.36(3)(12)⟩[c]<br>⟨7790.84(20)⟩[d] |
| | Fe XXIV | $[2s]_{1/2}$ | $[(1s\,2s)_1\,3p_{1/2}]_{3/2}$ | 7784.61(8)(29) | 7785.41 | 7784.43 | 7784[b]<br>⟨7785.03(6)(26)⟩[c] |
| (d) | Fe XXIII | $[2s\,2p_{1/2}]_1$ | $[1s\,3d_{5/2}]_2$ | 7691.50(26)(31) | 7692.84 | 7691.82 | |
| | Fe XXIII | $[2s^2]_0$ | $[1s\,3p_{1/2}]_1$ | 7711.80(82)(31) | 7712.68 | 7711.41 | |
| | Fe XXIII | $[2s^2]_0$ | $[1s\,3p_{3/2}]_1$ | 7721.65(6)(30) | 7722.47 | 7721.20 | 7721[b]<br>7722.23(58)[d] |
| | Fe XXIV | $[2p_{1/2}]_{1/2}$ | $[(1s\,2s)_1\,3s]_{1/2}$ | 7731.71(35)(30) | 7732.36 | 7731.35 | |
| (e) | Fe XXII | $[2p_{1/2}]_{1/2}$ | $[(1s\,2p_{1/2})_1\,3p_{3/2}]_{3/2}$ | 7624.65(14)(33) | 7627.28 | 7624.43 | |
| (f) | Fe XXI | $[2p^2]_0$ | $[1s\,3p_{3/2}]_1$ | 7528.58(13)(35) | 7531.70 | 7528.06 | |
| (g) | Fe XX | $[2p_{3/2}]_{3/2}$ | $\{[(1s\,2p_{1/2})_1\,2p^2]_2\,3p_{3/2}\}_{5/2}$ | ⟨7433.09(23)(37)⟩ | 7438.03 | 7433.96 | |

[a]Reference [11] (Theory).
[b]AtomDB [20].
[c]Reference [18] (Experiment).
[d]Reference [8] (Experiment).

TABLE V. Measured energies of the Fe $n > 3$ transitions. Experimental values in square brackets are used for calibration and set to literature values. For transitions with multiple strong transitions contributing almost equally, we just give the subshell occupation for the upper states. The corresponding fits are shown in Fig. 10. Angled brackets denote line blends with the nearby transitions marked with (*).

| RoI | Ion | Lower state | Upper state | Transition energy (eV) | Theory (eV) (pure CI) | Theory (eV) (MBPT) | Literature |
|---|---|---|---|---|---|---|---|
| (h) | Fe XXV | $[1s^2]_0$ | $[1s\,4p_{3/2}]_1$ | [8295.59(6)(28)] | 8294.78 | 8295.26 | 8295.482[a] 8295.67(1)(12)[b] |
| | Fe XXV | $[1s^2]_0$ | $[1s\,4p_{1/2}]_1$ | 8291.34(27)(28) | 8290.88 | 8291.36 | 8291.618[a] |
| (i) | Fe XXIV | $[2s]_{1/2}$ | $[(1s\,2s)_1\,4p_{1/2}]_{3/2}$ | 8181.35(27)(27) | 8182.33 | | |
| | Fe XXIV | $[2s]_{1/2}$ | $[(1s\,2s)_1\,4p_{3/2}]_{3/2}$ | 8184.96(12)(27) | 8185.39 | | |
| | Fe XXIV | $[2s]_{1/2}$ | $[(1s\,2s)_0\,4p_{3/2}]_{3/2}$ | 8215.41(14)(27) | 8215.56 | | |
| (j) | Fe XXIII | $[2s^2]_0$ | $[1s\,4p_{3/2}]_1$ | 8090.80(11)(26) | 8091.44 | | |
| (k) | Fe XXII | $[2p_{1/2}]_{1/2}$ | $[(1s\,2p_{1/2})_0\,4p_{1/2}]_{1/2}$ | 7962.78(52)(27) | 7965.84 | | |
| | Fe XXII | $[2p_{1/2}]_{1/2}$ | $[(1s\,2p_{1/2})_1\,4p_{3/2}]_{1/2}$ | ⟨7969.13(25)(27)⟩ | 7968.92 | | |
| | Fe XXII | $[2p_{1/2}]_{1/2}$ | $[(1s\,2p_{1/2})_0\,4p_{3/2}]_{3/2}$ | (*) | 7967.38 | | |
| (l) | Fe XXI | $[2p^2]_0$ | $[1s\,4p_{1/2}]_1$ | 7849.93(17)(28) | 7848.29 | | |
| (m) | Fe XXIV | $[2s]_{1/2}$ | $1s^1 2s^1 6p^1$ | ⟨8462.77(25)(34)⟩ | 8462.88 | | |
| | Fe XXV | $[1s^2]_0$ | $[1s\,5p_{3/2}]_1$ | [8487.43(6)(35)] | 8486.56 | 8487.09 | 8487.318[a] |
| (n) | Fe XXIV | $[2s]_{1/2}$ | $1s^1 2s^1 5p^1$ | ⟨8365.16(16)(30)⟩ | 8365.38 | | |
| | Fe XXIV | $[2s]_{1/2}$ | $1s^1 2s^1 5p^1$ | ⟨8395.25(31)(31)⟩ | 8395.73 | | |

[a]Reference [11] (Theory).
[b]Reference [18] (Experiment).


[1] P. Plucinsky, M. Agarwal, L. Gu, A. Foster, T. Sato, A. Bamba, J. Vink, M. Ichihashi, K. Matsunaga, K. Mori, H. Nakajima, F. S. Porter, H. Sonoda, S. Suzuki, D. Tateishi, Y. Terada, H. Uchida, and H. Yamaguchi, XRISM observations of Cassiopeia A: Overview, atomic data, and spectral models, Publ. Astron. Soc. Jpn. **77**, S171 (2025).

[2] M. Kurihara, M. Tsujimoto, M. Audard, E. Behar, L. Gu, K. Hamaguchi, N. Hell, C. A. Kilbourne, Y. Maeda, F. S. Porter, H. Sugai, and Y. Tsuboi, Spectroscopic diagnostics of high-temperature plasma in stellar coronae using Fe XXIV – XXIV K-shell lines with XRISM, Publ. Astron. Soc. Jpn. **77**, S50 (2025).

[3] M. Audard, H. Awaki, R. Ballhausen, A. Bamba, E. Behar, R. Boissay-Malaquin, L. Brenneman, G. V. Brown, L. Corrales, E. Costantini, R. Cumbee, M. D. Trigo, C. Done, T. Dotani, K. Ebisawa, M. Eckart, D. Eckert, T. Enoto, S. Eguchi, Y. Ezoe, *et al.*, Stratified wind from a super-Eddington X-ray binary is slower than expected, Nature (London) **646**, 57 (2025).

[4] A. Jerkstrand, F. Timmes, G. Magkotsios, S. Sim, C. Fransson, J. Spyromilio, B. Müller, A. Heger, J. Sollerman, and S. Smartt, Constraints on explosive silicon burning in core-collapse supernovae from measured Ni/Fe ratios, Astrophys. J. **807**, 110 (2015).

[5] D. Knapp, R. Marrs, M. Levine, C. Bennett, M. Chen, J. Henderson, M. Schneider, and J. Scofield, Dielectronic recombination of heliumlike nickel, Phys. Rev. Lett. **62**, 2104 (1989).

[6] H. Hsuan, M. Bitter, K. W. Hill, S. von Goeler, B. Grek, D. Johnson, L. C. Johnson, S. Sesnic, C. Bhalla, K. R. Karim, *et al.*, Satellite Spectra of Heliumlike Nickel (Plasma Physics Lab, Princeton University, NJ, USA, 1987), URL: https://inis.iaea.org/records/ermwz-xgw43.

[7] M. Bitter, H. Hsuan, V. Decaux, B. Grek, K. W. Hill, R. Hulse, L. A. Kruegel, D. Johnson, S. von Goeler, and M. Zarnstorff, Satellite spectra of the $K\alpha$ resonance line of heliumlike nickel, Ni XXVII, from tokamak-fusion-test reactor plasmas: Comparison between theory and experiment, Phys. Rev. A **44**, 1796 (1991).

[8] A. Smith, M. Bitter, H. Hsuan, K. Hill, S. von Goeler, J. Timberlake, P. Beiersdorfer, and A. Osterheld, $K\beta$ spectra of heliumlike iron from tokomak-fusion-test-reactor plasmas, Phys. Rev. A **47**, 3073 (1993).

[9] F. Bombarda, R. Giannella, E. Källne, G. Tallents, F. Bely-Dubau, P. Faucher, M. Cornille, J. Dubau, and A. Gabriel, Observations and comparisons with theory of the heliumlike and hydrogenlike resonance lines and satellites of nickel from the JET tokamak, Phys. Rev. A **37**, 504 (1988).

[10] L. Natarajan and R. Kadrekar, Radiative decay from doubly and singly excited states of He-like nickel, Phys. Rev. A **88**, 012501 (2013).

[11] V. A. Yerokhin and A. Surzhykov, Theoretical energy levels of $1sns$ and $1snp$ states of helium-like ions, J. Phys. Chem. Ref. Data **48**, 033104 (2019).

[12] V. Yerokhin and A. Surzhykov, Energy levels of core-excited $1s2l2l'$ states in lithium-like ions: Argon to uranium, J. Phys. Chem. Ref. Data **47**, 023105 (2018).

[13] P. Palmeri, P. Quinet, C. Mendoza, M. A. Bautista, J. García, M. C. Witthoeft, and T. R. Kallman, Radiative and Auger decay

data for modeling nickel K lines, Astrophys. J. Suppl. Ser. **179**, 542 (2008).

[14] R. D. Cowan, *The Theory of Atomic Structure and Spectra* (University of California Press, Berkely, CA, 2023), Vol. 3.

[15] J. K. Rudolph, S. Bernitt, S. W. Epp, R. Steinbrügge, C. Beilmann, G. V. Brown, S. Eberle, A. Graf, Z. Harman, N. Hell, M. Leutenegger, A. Müller, K. Schlage, H.-C. Wille, H. Yavaş, J. Ullrich, and J. R. C. López-Urrutia, X-ray resonant photoexcitation: Linewidths and energies of $K\alpha$ transitions in highly charged Fe ions, Phys. Rev. Lett. **111**, 103002 (2013).

[16] R. Steinbrügge, S. Kühn, F. Nicastro, M. F. Gu, M. Togawa, M. Hoesch, J. Seltmann, I. Sergeev, F. Trinter, S. Bernitt, C. Shah, M. A. Leutenegger, and J. R. C. López-Urrutia, X-ray photoabsorption of density-sensitive metastable states in Ne VII, Fe XXII, and Fe XXIII, Astrophys. J. **941**, 188 (2022).

[17] V. Decaux, P. Beiersdorfer, A. Osterheld, M. Chen, and S. Kahn, High-resolution measurements of the K alpha spectra of low-ionization species of iron: A new spectral signature of nonequilibrium ionization conditions in young supernova remnants, Astrophys. J. **443**, 464 (1995).

[18] J. K. Rudolph, Fluoreszenzspektroskopie an K-Schalen-Übergängen hochgeladener Eisenionen, Ph.D. thesis, Gießen, Justus-Liebig-Universität, 2013.

[19] J. Kaastra, A. Raassen, J. De Plaa, and L. Gu, SPEX X-ray spectral fitting package (Version 3.06.01) [Computer software], Zenodo, 2020, URL: https://doi.org/10.5281/zenodo.4384188.

[20] A. Foster, L. Ji, R. Smith, and N. Brickhouse, Updated atomic data and calculations for X-ray spectroscopy, Astrophys. J. **756**, 128 (2012).

[21] M. Cruise, M. Guainazzi, J. Aird, F. J. Carrera, E. Costantini, L. Corrales, T. Dauser, D. Eckert, F. Gastaldello, H. Matsumoto, R. Osten, P.-O. Petrucci, D. Porquet, G. W. Pratt, N. Rea, T. H. Reiprich, A. Simionescu, D. Spiga, and E. Troja, The NewAthena mission concept in the context of the next decade of X-ray astronomy, Nat. Astron. **9**, 36 (2025).

[22] D. Barret, V. Albouys, J.-W. d. Herder, L. Piro, M. Cappi, J. Huovelin, R. Kelley, J. M. Mas-Hesse, S. Paltani, G. Rauw, A. Rozanska, J. Svoboda, J. Wilms, N. Yamasaki, M. Audard, S. Bandler, M. Barbera, X. Barcons, E. Bozzo, M. T. Ceballos, *et al.*, The Athena X-ray integral field unit: A consolidated design for the system requirement review of the preliminary definition phase, Exp. Astron. **55**, 373 (2023).

[23] L. Ravera, D. Barret, J. W. den Herder, L. Piro, R. Clédassou, E. Pointecouteau, P. Peille, F. Pajot, M. Arnaud, C. Pigot, *et al.*, *Space Telescopes and Instrumentation 2014: Ultraviolet to Gamma Ray* (SPIE, Bellingham, WA, 2014), Vol. 9144, pp. 779–791.

[24] P. Peille, D. Barret, E. Cucchetti, V. Albouys, L. Piro, A. Simionescu, M. Cappi, E. Bellouard, C. Cénac-Morthé, C. Daniel, A. Pradines, A. Finoguenov, R. Kelley, J. M. Mas-Hesse, S. Paltani, G. Rauw, A. Rozanska, J. Svoboda, J. Wilms, M. Audard, *et al.*, The X-ray integral field unit at the end of the Athena reformulation phase, Exp. Astron. **59**, 18 (2025).

[25] S. W. Epp, J. R. C. López-Urrutia, M. C. Simon, T. Baumann, G. Brenner, R. Ginzel, N. Guerassimova, V. Mäckel, P. H. Mokler, B. L. Schmitt, H. Tawara, and J. Ullrich, X-ray laser spectroscopy of highly charged ions at FLASH, J. Phys. B: At. Mol. Opt. Phys. **43**, 194008 (2010).

[26] S. Epp, Röntgen-laserspektroskopie hochgeladener ionen in einer EBIT am freie-elektronen-laser flash, Ph.D. thesis, Ruprecht-Karls Universität Heidelberg, 2007.

[27] D. Vaccaro, H. Akamatsu, L. Gottardi, M. de Wit, M. P. Bruijn, J. van der Kuur, K. Nagayoshi, E. Taralli, K. Ravensberg, J.-R. Gao, and J. W. A. den Herder, Developments on frequency domain multiplexing readout for large arrays of transition-edge sensor X-ray micro-calorimeters, J. Low Temp. Phys. **216**, 21 (2024).

[28] M. Botz, C. Shah, L. Gottardi, M. de Wit, L. Gu, J. Danisch, F. Pajot, T. Pfeifer, and J. R. C. López-Urrutia, High-resolution charge-exchange spectroscopy of $Si^{13+/14+}$ ions with an X-ray microcalorimeter, Eur. Phys. J.: Spec. Top. **235**, 3457 (2026).

[29] V. Yerokhin and V. Shabaev, Lamb shift of $n = 1$ and $n = 2$ states of hydrogen-like atoms, $1 \leqslant Z \leqslant 110$, J. Phys. Chem. Ref. Data **44**, 033103 (2015).

[30] M. Botz, L. Gu, M. de Wit, L. Gottardi, C. Shah, F. Pajot, T. Pfeifer, and J. R. C. López-Urrutia, Determination of transition energies and excitation cross sections of Rydberg transitions in S XV and S XVI using a transition edge sensor microcalorimeter, Astrophys. J. **1005**, 232 (2026).

[31] M. F. Gu, The flexible atomic code, Can. J. Phys. **86**, 675 (2008).

[32] M. Gu, Wavelengths of $2\ l \rightarrow 3\ l'$ transitions in L-shell ions of iron and nickel: A combined configuration interaction and many-body perturbation theory approach, Astrophys. J. Suppl. Ser. **156**, 105 (2005).

[33] M. Safronova, W. Johnson, and U. Safronova, Relativistic many-body calculations of the energies of $n = 2$ states for the berylliumlike isoelectronic sequence, Phys. Rev. A **53**, 4036 (1996).

[34] M. J. Vilkas, Y. Ishikawa, and K. Koc, Relativistic multireference many-body perturbation theory for quasidegenerate systems: Energy levels of ions of the oxygen isoelectronic sequence, Phys. Rev. A **60**, 2808 (1999).

[35] J. S. Kaastra, On the use of C-stat in testing models for X-ray spectra, Astron. Astrophys. **605**, A51 (2017).

[36] A. Kramida, Y. Ralchenko, J. Reader, and N. A. Team, NIST atomic spectra database (version 5.12), National Institute of Standards and Technology, Gaithersburg, MD, 2024, DOI: https://dx.doi.org/10.18434/T4W30F.

[37] C. A. Kilbourne, S. Bandler, A.-D. Brown, J. Chervenak, E. Figueroa-Feliciano, F. Finkbeiner, N. Iyomoto, R. Kelley, F. Porter, and S. Smith, Various optimizations of TES arrays for X-ray astrophysics, J. Low Temp. Phys. **151**, 223 (2008).

[38] G. C. O'Neil, P. Szypryt, E. Takacs, J. N. Tan, S. W. Buechele, A. S. Naing, Y. I. Joe, D. Swetz, D. R. Schmidt, W. B. Doriese, J. D. Gard, C. D. Reintsema, J. N. Ullom, J. S. Villarrubia, and Y. Ralchenko, On low-energy tail distortions in the detector response function of X-ray microcalorimeter spectrometers, J. Low Temp. Phys. **199**, 1046 (2020).

[39] V. Azarov, A. Kramida, and Y. Ralchenko, A critical compilation of experimental data on the $1s2\ l2l'$ core-excited states of Li-like ions from carbon to uranium, At. Data Nucl. Data Tables **149**, 101548 (2023).